Monthly Notices
of the
ROYAL ASTRONOMICAL SOCIETY

MNRAS **451,** 3975–3985 (2015) doi:10.1093/mnras/stv1252

Radio polarimetry as a probe of unresolved jets: the 2013 outburst of XTE J1908+094

P. A. Curran,[1⋆] J. C. A. Miller-Jones,[1] A. P. Rushton,[2,3] D. D. Pawar,[4] G. E. Anderson,[2] D. Altamirano,[3] H. A. Krimm,[5,6] J. W. Broderick,[2] T. M. Belloni,[7] R. P. Fender,[2] E. G. Körding,[8] D. Maitra,[9] S. Markoff,[10] S. Migliari,[11,12] C. Rumsey,[13] M. P. Rupen,[14] D. M. Russell,[15] T. D. Russell,[1] C. L. Sarazin,[16] G. R. Sivakoff,[17] R. Soria,[1] A. J. Tetarenko,[17] D. Titterington[13] and V. Tudose[18]

[1]*International Centre for Radio Astronomy Research, Curtin University, GPO Box U1987, Perth, WA 6845, Australia*
[2]*Department of Physics, University of Oxford, Keble Road, Oxford OX1 3RH, UK*
[3]*School of Physics and Astronomy, University of Southampton, Southampton, Hampshire, SO17 1BJ, UK*
[4]*Department of Physics, R. J. College, Ghatkopar (W), Mumbai 400086, India*
[5]*Universities Space Research Association, Columbia, MD 21044, USA*
[6]*NASA/Goddard Space Flight Center, Astrophysics Science Division, Code 661, Greenbelt, MD 20771, USA*
[7]*INAF – Osservatorio Astronomico di Brera, Via E. Bianchi 46, I-23807 Merate (LC), Italy*
[8]*Department of Astrophysics/IMAPP, Radboud University Nijmegen, PO Box 9010, NL-6500 GL Nijmegen, the Netherlands*
[9]*Department of Physics and Astronomy, Wheaton College, Norton, MA 02766, USA*
[10]*Astronomical Institute 'Anton Pannekoek', University of Amsterdam, PO Box 94249, NL-1090 GE Amsterdam, the Netherlands*
[11]*XMM-Newton Science Operations Centre, ESAC/ESA, PO Box 78, E-28691 Villanueva de la Cañada, Madrid, Spain*
[12]*Department of Astronomy and Meteorology & ICCUB, University of Barcelona, Martí i Franquès 1, E-08028 Barcelona, Spain*
[13]*Astrophysics Group, Cavendish Laboratory, 19 JJ Thomson Avenue, Cambridge CB3 0HE, UK*
[14]*National Research Council, Herzberg Astronomy and Astrophysics, 717 White Lake Road, PO Box 248, Penticton, BC V2A 6J9, Canada*
[15]*New York University Abu Dhabi, PO Box 129188, Abu Dhabi, United Arab Emirates*
[16]*Department of Astronomy, University of Virginia, PO Box 400325, Charlottesville, VA 22904, USA*
[17]*Department of Physics, University of Alberta, 4-181 CCIS, Edmonton, AB T6G 2E1, Canada*
[18]*Institute for Space Sciences, Atomistilor 409, PO Box MG-23, Bucharest-Măgurele RO-077125, Romania*

Accepted 2015 June 2. Received 2015 June 1; in original form 2015 March 03

ABSTRACT

XTE J1908+094 is an X-ray transient black hole candidate in the Galactic plane that was observed in outburst in 2002 and 2013. Here we present multifrequency radio and X-ray data, including radio polarimetry, spanning the entire period of the 2013 outburst. We find that the X-ray behaviour of XTE J1908+094 traces the standard black hole hardness–intensity path, evolving from a hard state, through a soft state, before returning to a hard state and quiescence. Its radio behaviour is typical of a compact jet that becomes quenched before discrete ejecta are launched during the late stages of X-ray softening. The radio and X-ray fluxes, as well as the light-curve morphologies, are consistent with those observed during the 2002 outburst of this source. The polarization angle during the rise of the outburst infers a jet orientation in agreement with resolved observations but also displays a gradual drift, which we associate with observed changes in the structure of the discrete ejecta. We also observe an unexpected 90° rotation of the polarization angle associated with a second component.

Key words: binaries: close – stars: individual: XTE J1908+094 – X-rays: binaries – X-rays: bursts.

1 INTRODUCTION

Relativistic jets are a standard feature of black holes in both actively accreting (e.g. Mirabel & Rodríguez 1998; Fender 2006) and quiescent (e.g. Gallo et al. 2006) low-mass X-ray binary (LMXB) systems. The evolution of the bipolar jets during an outburst event is dependent on the accretion rate on to the black hole (Fender 2006) and is closely coupled with the observed X-ray 'states' (see e.g. McClintock & Remillard 2006; Belloni 2010). During the *hard* X-ray state of a standard LMXB outburst (when the X-ray spectrum is dominated by power-law emission from the optically thin, geometrically thick inner regions), radio emission from compact,

⋆E-mail: peter.curran@curtin.edu.au

partially self-absorbed, flat-spectrum ($\alpha \sim 0$, where $F_\nu \propto \nu^\alpha$) jets is often observed. The radio emission of the compact jets increases in luminosity, from quiescent levels, before being quenched by a factor of at least ∼700 (e.g. Coriat et al. 2011; Russell et al. 2011) at, or around, the X-ray peak of the outburst – corresponding to the transition to the *soft* X-ray state (where the X-ray spectrum is dominated by a thermal blackbody component from the accretion disc). During this transition to the soft state, defined by various classes of *intermediate* X-ray states, the overall radio emission is observed to become optically thin ($\alpha < 0$) and, occasionally, to exhibit flares (though these may be easily missed due to low-cadence radio observations). In fact, in a number of sources, this optically thin emission has been spatially resolved as discrete ejecta (e.g. Tingay et al. 1995; Mirabel & Rodríguez 1998; Miller-Jones et al. 2012). However, it is also worth noting that in some cases – such as the 2010 outburst of MAXI J1659−152, which was observed to transition to a full soft state – no evidence of discrete ejecta was detected despite being well sampled at the time (Paragi et al. 2013; van der Horst et al. 2013). Finally, towards the end of the outburst, when the X-ray luminosity decreases to approximately 2 per cent of the Eddington luminosity (Maccarone 2003; Dunn et al. 2010; Kalemci et al. 2013), the compact jets are reestablished and seen to fade with X-ray luminosity.

Optically thin radio emission from the discrete ejecta can, in the presence of an ordered magnetic field, be linearly polarized at a level of up to ≈70 per cent (Longair 1994). The flat-spectrum compact jets can reach a fraction of this, depending on the underlying distribution of synchrotron spectra. However, the magnetic field is not necessarily ordered and a number of mechanisms – such as multiple, unresolved components that cancel each other out, or spatially dependent Faraday rotation – can suppress the resulting net polarization (see e.g. Brocksopp et al. 2007 and references therein). Most LMXBs with published fractional polarizations have been observed at much lower levels of $\lesssim$10 per cent (e.g. Fender 2003 and references therein; Brocksopp et al. 2007) with relatively few having fractional polarizations of ≈50 per cent (Brocksopp et al. 2013; Curran et al. 2014). When detected, polarization can be used to infer properties of the magnetic field and the surrounding medium (e.g. Stirling et al. 2004; Miller-Jones et al. 2008), as well as properties of the jet itself. An alignment between the compact jet axis and the intrinsic polarization angle has now been observed in a number of sources (e.g. Corbel et al. 2000; Russell & Shahbaz 2014; Russell et al. 2015) and, if common to all black hole X-ray LMXBs, this allows us to infer the orientation of unresolved compact jets.

1.1 XTE J1908+094

The transient X-ray source, XTE J1908+094, was first detected on 2002 February 21 (MJD 52326) by the Proportional Counter Array aboard the *Rossi X-ray Timing Explorer* (*RXTE*) satellite (Woods et al. 2002). Very Large Array (VLA) radio observations on 2002 March 21 (Rupen, Mioduszewski & Dhawan 2002) refined the position in the Galactic plane (l, b = 43.°26, +0.°43), to sub-arcsecond precision,[1] as RA, Dec. = 19:08:53.077, +09:23:04.9 ± 0.1″(J2000). Further VLA observations identified discrete ejecta, moving along the north–north-west direction.[2] Two possible near-infrared counterparts were identified consistent with this position (Chaty, Mignani & Vanzi 2002; Chaty, Mignani &xbrk Israel 2006).[3] On the basis of X-ray timing and spectral properties, including the detection of quasi-periodic oscillations in the power spectrum, the source was classified as a black hole candidate that exhibited both hard and soft states (in't Zand et al. 2002; Göğüş et al. 2004). Furthermore, limited quasi-simultaneous radio (VLA and Westerbork Synthesis Radio Telescope) and X-ray (*RXTE*) observations were found to be consistent with the expected hard state correlation of black holes (e.g. Gallo, Fender & Pooley 2003) by Jonker et al. (2004).

XTE J1908+094 was next detected in outburst on 2013 October 26 (MJD 56591) by the Burst Alert Telescope (BAT) on the *Swift* satellite (Krimm et al. 2013b) and further detected by both the *Swift* X-ray Telescope (XRT) and the Monitor of All-sky X-ray Image (MAXI) instrument aboard the *International Space Station* (Krimm, Kennea & Holland 2013c; Negoro et al. 2013). A radio counterpart was detected at frequencies from 5 to 22 GHz at the Karl G. Jansky VLA (Miller-Jones, Sivakoff & Krimm 2013), the Arcminute Microkelvin Imager Large Array (AMI-LA; Rushton et al. 2013), the Australia Telescope Compact Array (Coriat et al. 2013), the Very Long Baseline Array (VLBA) and the European VLBI Network (EVN; Rushton et al., in preparation). Rushton et al. (in preparation) also confirm the 2002 direction of jet motion along the north–north-west direction as well as identifying an expanding southern component that fades to background levels and is superseded by a northern component on MJD 56607. Here we present our VLA, Low-Frequency Array (LOFAR) and AMI-LA observations combined with X-ray monitoring of the 2013 outburst of XTE J1908+094. In Section 2 we introduce the observations and reduction methods, while in Section 3 we discuss the results of our photometric and polarimetric analyses of the data and discuss their physical implications for the system. We summarize our findings in Section 4.

2 OBSERVATIONS AND ANALYSIS

2.1 Radio data

2.1.1 VLA

XTE J1908+094 was observed by the VLA from 2013 October 29 to November 22 (15 epochs in B configuration) and again on 2014 March 11 and 22 in A configuration (see Table 1). Observations were primarily made at central frequencies of 5.25 and 7.45 GHz; each baseband was comprised of eight spectral windows with sixty-four 2 MHz channels each, giving a bandwidth of 1.024 GHz per baseband. Further observations were obtained in the 18–26 GHz band (central frequency of 22 GHz) using eight 1.024 GHz basebands, as above. Additionally, on three epochs observations were made in the 1–2 GHz band, which has 16 spectral windows with sixty-four 1 MHz channels each. The 1–2 GHz band is heavily affected by radio frequency interference that reduced the usable spectral windows to between 5 and 6 (≈320 MHz), spread over the band, which was treated as a whole. This led to a total bandwidth of ≈500 MHz with an effective frequency of 1.6 GHz.

Flagging, calibration and imaging of the data followed standard procedures and were carried out within the Common Astronomy

[1] All uncertainties in this paper are quoted and/or plotted at the 1σ confidence level.

[2] http://www.aoc.nrao.edu/∼mrupen/XRT/X1908+094/x1908+094.shtml

[3] Note that these authors misquote the RA as 19:08:53.77, though have used the correct position when identifying the counterpart.

Table 1. Radio flux densities of source, F_ν, at frequency, ν, and Stokes Q and U flux densities or 3σ upper limit on polarization, $P_{\rm limit}$, at 5.25 and 7.45 GHz (statistical errors only). Additional 15.7 GHz data, plotted in Fig. 1, are not tabulated but have 3σ upper limits of <0.24 mJy.

Epoch (MJD)	ν (GHz)	F_ν (mJy)	Q (mJy beam^{-1})	U (mJy beam^{-1})	$P_{\rm limit}$ (mJy beam^{-1})
56594.968	5.25	0.76 ± 0.02	–	–	<0.07
56594.968	7.45	0.70 ± 0.02	–	–	<0.06
56595.700	15.7	0.83 ± 0.08	–	–	–
56596.750	15.7	1.21 ± 0.06	–	–	–
56597.700	15.7	1.62 ± 0.06	–	–	–
56599.700	15.7	1.41 ± 0.07	–	–	–
56600.700	15.7	1.11 ± 0.07	–	–	–
56601.078	5.25	0.52 ± 0.02	–	–	<0.07
56601.078	7.45	0.48 ± 0.03	–	–	<0.08
56601.700	15.7	9.29 ± 0.09	–	–	–
56602.700	15.7	<0.32	–	–	–
56603.062	5.25	1.27 ± 0.03	0.069 ± 0.025	0.103 ± 0.025	–
56603.062	7.45	1.14 ± 0.04	–	–	<0.10
56603.649	0.145	<9.3	–	–	–
56603.700	15.7	0.67 ± 0.08	–	–	–
56604.026	5.25	2.52 ± 0.04	−0.034 ± 0.028	−0.203 ± 0.028	–
56604.026	7.45	2.33 ± 0.04	−0.058 ± 0.032	0.194 ± 0.031	–
56604.700	15.7	3.03 ± 0.11	–	–	–
56604.958	22	2.45 ± 0.03	–	–	–
56605.076	5.25	4.73 ± 0.04	−0.380 ± 0.026	−0.341 ± 0.026	–
56605.076	7.45	4.00 ± 0.04	0.153 ± 0.031	0.521 ± 0.030	–
56605.700	15.7	10.40 ± 0.10	–	–	–
56606.700	15.7	12.91 ± 0.07	–	–	–
56606.918	22	11.47 ± 0.04	–	–	–
56607.070	5.25	13.43 ± 0.11	−0.120 ± 0.026	−0.091 ± 0.025	–
56607.070	7.45	12.96 ± 0.10	0.158 ± 0.035	0.289 ± 0.035	–
56607.700	15.7	4.63 ± 0.12	–	–	–
56608.050	22	4.71 ± 0.03	–	–	–
56608.098	5.25	6.72 ± 0.07	0.237 ± 0.028	0.287 ± 0.029	–
56608.098	7.45	6.14 ± 0.06	0.045 ± 0.033	−0.320 ± 0.033	–
56608.635	0.145	<12.5	–	–	–
56608.700	15.7	2.74 ± 0.08	–	–	–
56609.048	22	2.32 ± 0.02	–	–	–
56609.065	5.25	3.33 ± 0.04	0.133 ± 0.025	0.098 ± 0.026	–
56609.065	7.45	3.05 ± 0.04	−0.087 ± 0.029	−0.129 ± 0.028	–
56609.700	15.7	1.24 ± 0.08	–	–	–
56610.045	22	1.27 ± 0.03	–	–	–
56610.062	5.25	2.22 ± 0.03	–	–	<0.08
56610.062	7.45	2.04 ± 0.03	–	–	<0.08
56610.700	15.7	0.51 ± 0.07	–	–	–
56611.042	22	0.58 ± 0.02	–	–	–
56611.601	0.145	<12.6	–	–	–
56611.700	15.7	0.49 ± 0.07	–	–	–
56612.040	1.6	2.09 ± 0.24	–	–	–
56612.078	5.25	0.98 ± 0.06	–	–	<0.17
56612.078	7.45	0.91 ± 0.07	–	–	<0.21
56614.597	0.145	<13.5	–	–	–
56614.700	15.7	<0.30	–	–	–
56615.700	15.7	<0.24	–	–	–
56616.004	5.25	0.38 ± 0.05	–	–	<0.14
56616.004	7.45	0.29 ± 0.05	–	–	<0.15
56616.008	1.6	0.92 ± 0.08	–	–	–
56616.029	22	0.14 ± 0.03	–	–	–
56616.700	15.7	<0.43	–	–	–
56617.700	15.7	<0.24	–	–	–
56617.999	5.25	0.36 ± 0.03	–	–	<0.07
56617.999	7.45	0.27 ± 0.03	–	–	<0.09
56618.020	1.6	0.53 ± 0.03	–	–	–
56618.700	15.7	<0.24	–	–	–
56727.532	5.25	0.09 ± 0.02	–	–	<0.05
56727.533	7.45	0.09 ± 0.02	–	–	<0.05
56738.694	5.25	<0.07	–	–	–
56738.694	7.45	<0.09	–	–	–

Software Application (CASA 4.2.1) package (McMullin et al. 2007). The primary calibrator used as the bandpass and polarization angle calibrator, and to set the amplitude scale at all frequencies, was either 3C48 (J0137+331) or 3C286 (J1331+3030), depending on the local sidereal time of the observations. J1824+1044 was used as the secondary (phase) calibrator at 1.6 GHz, J1922+1530 was used at 5.25 and 7.45 GHz and J1856+0610 was used at 22 GHz. The polarization leakage calibrator at 5.25 and 7.45 GHz

was J2355+4950, except on 2014 March 11 when J1407+2827 was used.

Images were generated with robust = 0 weighting and phase self-calibration was performed on a per-band basis, or for 5.25 and 7.45 GHz on a per-baseband or per-spectral window basis depending on the signal-to-noise ratio (though we only tabulate results at the central frequencies of the basebands). The flux densities of the source were measured by fitting a point source in the image plane (Stokes *I*), and, as is usual for VLA data, systematic errors of 1 per cent should be added at frequencies <10 GHz and 3 per cent at 22 GHz. At 5.25 and 7.45 GHz, Stokes *Q* and *U* flux densities were measured at peak (Table 1).

2.1.2 AMI-LA

AMI-LA observed XTE J1908+094 from 2013 October 30 to 2014 March 22, with a cadence of between 1–4 d. Each epoch lasted approximately 4 h, centred around the local sidereal time of the peak elevation of the source. AMI-LA consists of 8 × 12.8 m antennas with baselines ranging from 18 to 110 m, located at the Mullard Radio Astronomy Observatory in the UK (AMI Consortium: Zwart et al. 2008). AMI-LA has an operational range of 13.9–17.5 GHz when using frequency channels 3–7, each with a bandwidth of 0.72 GHz (channels 2, 3 and 8 are disregarded due to their current susceptibility to interference). This gives a total usable bandwidth of ∼3.6 GHz, centred at 15.7 GHz.

Initial data reduction was performed with the PYTHON `drive-ami` pipeline (Staley et al. 2013). `drive-ami` utilizes the REDUCE software package, which is designed to take the raw AMI-LA data and automatically flag for interference, shadowing and hardware errors, conduct phase and amplitude calibrations, and Fourier transforms the data into *uv*-FITS format (Perrott et al. 2013). Short, interleaved observations of J1856+0610 were used for phase calibration. Imaging was conducted using the `chimenea` data reduction pipeline that has been specifically designed to deal with multi-epoch radio observations of transients (Staley & Anderson 2015). The resulting peak AMI-LA flux densities of XTE J1908+094 (Table 1) were measured using MIRIAD (Sault, Teuben & Wright 1995) and systematic errors of 5 per cent (Perrott et al. 2013) should be added in quadrature. Note that the flux errors may be underestimated due to uncleanable artefacts resulting from the nearby off-axis radio-bright source that may be associated with the star-forming region W49A (Webster, Altenhoff & Wink 1971). For further details on the reduction and analysis performed on the AMI observations, see Anderson et al. (2014).

2.1.3 LOFAR

LOFAR (van Haarlem et al. 2013) observed XTE J1908+094 on four epochs over the period 2013 November 7–18. Observations were obtained with the high-band antennas from 115 to 189 MHz, using 380 sub-bands, each with a bandwidth of 195.3 kHz. Each observation consisted of 20 min snapshots of the field, interleaved with 1.5 min scans of the primary calibrator, 3C380, for a total of 160 min on source in all epochs, except the second observation where the total was 80 min. The runs were mainly carried out during the daytime, and included transit; the minimum source elevation across all four observations was about 39°. Flagging, calibration and imaging followed standard methods (e.g. Heald et al. 2011; Offringa et al. 2012; van Haarlem et al. 2013) while amplitude calibration was based on the 3C380 model from Scaife & Heald (2012). We performed phase-only calibration on the target field using a local sky model determined by cross-correlating the 74 MHz VLA Low-Frequency Sky Survey (Cohen et al. 2007) with the 1.4 GHz NRAO VLA Sky Survey (Condon et al. 1998). Sub-bands were combined into six, approximately evenly split bands and an image was generated for each band with the task AWIMAGER (Tasse et al. 2013), using robust = 0 weighting. These were then convolved to a common resolution and averaged, using inverse-variance weighting, to produce a final image. The projected baseline range was restricted to 0.1–6 $k\lambda$ (maximum baseline approximately 12 km in the centre of the band). Although we used the full Dutch array in our observations, at the time of writing, long baseline imaging was not routine with simple, computationally inexpensive calibration procedures such as the one we have adopted here. The minimum baseline cutoff was empirically determined so as to reduce the confusion limit due to extended emission along the Galactic plane. The effective frequency of each image is about 145 MHz, and the average angular resolution is 55 arcsec × 33 arcsec (with a beam position angle of ≈30°). No source was detected at the position of XTE J1908+094, on any epoch, above the flux limits given in Table 1.

2.2 X-ray data

We analysed 38 *Swift*/XRT Windowed Timing (WT) observations of XTE J1908+094 obtained from 2013 October 29 to December 3 and from 2014 February 15 to March 17 (Table 2). Between these dates, XRT observations were not possible due to the position of the Sun (i.e. source was Sun-constrained). Due to the known issue of low-energy spectral residuals in WT data for heavily absorbed sources,[4] we extracted source and background spectra in the 1.5–10 keV range only (grades 0–2), using suitable extraction regions of radius ∼75 arcsec. Ancillary response files were generated using the FTOOL `xrtmkarf` and the response matrix available at the time of observations. Spectra were rebinned to have a minimum of 20 counts per bin (so that χ^2 statistics are valid) and analysed within XSPEC (version: 12.8.0), though two late epochs did not have enough counts to produce useful spectra (*Swift* Obs IDs 00033014037 and 039).

Due to low count rates and the relatively high low-energy cutoff at 1.5 keV, we are unable to consistently distinguish between the physically motivated absorbed multicoloured blackbody plus power-law model (`tbabs*(diskbb+pow)`) and the single absorbed power-law model (`tbabs*powerlaw`). Therefore, we opt to fit a phenomenological power-law model (`tbabs*powerlaw`), purely to calculate the flux from 3.0 to 9.0 keV (Table 2, Fig. 1) and, via the photon index, to indicate the X-ray state of the system. WT mode data are unaffected by pile-up. The absorption, $N_{\rm H}$, was in the range 1.5–3.0 × 10^{22} $\rm cm^{-2}$ (consistent with the value found by in't Zand et al. 2002) and the reduced χ^2 varied from 0.78 to 1.96, with a mean value of 1.29.

Hard X-ray (15–50 keV) light curves (counts/s) were obtained by the *Swift*/BAT transient monitor[5] (Krimm et al. 2013a). The data points are based on daily average results from the monitor, which have been binned so that each point either has a significance of $>3\sigma$ or covers a period of 7 d (Fig. 1). For comparison, MAXI (Matsuoka et al. 2009) light curves were downloaded[6] but due to the

[4] http://www.swift.ac.uk/analysis/xrt/digest_cal.php#abs
[5] http://swift.gsfc.nasa.gov/docs/swift/results/transients
[6] http://maxi.riken.jp

Table 2. *Swift* observation ID, ObsID, XRT X-ray fluxes of source from 3 to 9 keV, $F_{X[3-9\,\mathrm{keV}]}$ and the photon index of the power-law fit to spectra, Γ.

Epoch (MJD)	ObsID	$F_{X[3-9\,\mathrm{keV}]}$ ($\times 10^{-10}$ erg cm^{-2} s^{-1})	Γ
56594.84	33014001	7.23 ± 0.19	1.80 ± 0.07
56597.91	33014002	11.70 ± 0.20	2.12 ± 0.05
56599.53	33014003	14.60 ± 0.23	2.84 ± 0.05
56604.85	33014004	13.80 ± 0.23	4.71 ± 0.05
56605.80	33014005	13.20 ± 0.23	4.73 ± 0.05
56606.05	33014006	15.10 ± 0.34	4.61 ± 0.08
56607.39	33014007	14.50 ± 0.24	4.44 ± 0.06
56608.05	33014008	13.40 ± 0.21	4.49 ± 0.06
56609.19	33014009	10.20 ± 0.17	4.91 ± 0.06
56610.79	33014010	11.40 ± 0.24	4.97 ± 0.07
56611.33	33014011	7.57 ± 0.17	5.08 ± 0.07
56612.60	33014012	11.70 ± 0.21	4.97 ± 0.06
56614.40	33014014	9.18 ± 0.19	5.04 ± 0.07
56615.73	33014015	8.74 ± 0.18	4.86 ± 0.07
56616.13	33014016	8.88 ± 0.18	4.95 ± 0.07
56619.06	33014017	8.06 ± 0.18	5.03 ± 0.07
56624.47	33014018	7.39 ± 0.17	4.86 ± 0.08
56629.00	33014019	7.79 ± 0.16	5.11 ± 0.07
56703.93	33014020	1.13 ± 0.09	2.36 ± 0.18
56704.67	33014021	1.07 ± 0.06	2.44 ± 0.15
56705.87	33014022	1.09 ± 0.06	1.84 ± 0.15
56706.67	33014023	1.08 ± 0.05	2.11 ± 0.12
56708.67	33014024	1.02 ± 0.02	2.13 ± 0.17
56713.00	33014025	0.83 ± 0.11	2.23 ± 0.25
56713.13	33014026	1.28 ± 0.06	1.67 ± 0.23
56713.20	33014027	0.64 ± 0.01	1.52 ± 0.23
56715.13	33014028	0.55 ± 0.05	1.79 ± 0.22
56717.46	33014029	0.54 ± 0.07	1.82 ± 0.23
56718.74	33014030	0.68 ± 0.12	2.03 ± 0.28
56719.33	33014031	0.65 ± 0.10	1.72 ± 0.27
56721.72	33014032	0.53 ± 0.06	1.41 ± 0.24
56723.73	33014033	0.66 ± 0.10	1.99 ± 0.28
56723.19	33014034	0.57 ± 0.08	1.46 ± 0.24
56725.93	33014035	0.47 ± 0.08	1.89 ± 0.28
56727.06	33014036	0.43 ± 0.08	1.94 ± 0.32
56729.08	33014038	0.38 ± 0.07	1.43 ± 0.32

source's proximity to the bright, persistent source GRS 1915+105, these may suffer from contamination, especially at low luminosities (Negoro et al. 2013).

2.3 Radio spectral indices

We obtain the spectral index, α (where $F_\nu \propto \nu^\alpha$), of the radio spectrum at each epoch with multiple observed frequencies by fitting a power law to the derived flux densities, F_ν, against frequency, ν. Due to the short time-scale variability of this source (Section 3.1), we use only data which are simultaneous, i.e. the VLA data. The flux densities over the entire 1.6 and 22 GHz bands were used along with the flux densities at 5.25 and 7.45 GHz on a per-baseband or, for the brighter epochs, a per-spectral window basis. We obtain similar values for the spectral indices using both the per-baseband and per-spectral window flux densities. All epochs were well fitted by a single power law with no need for additional components.

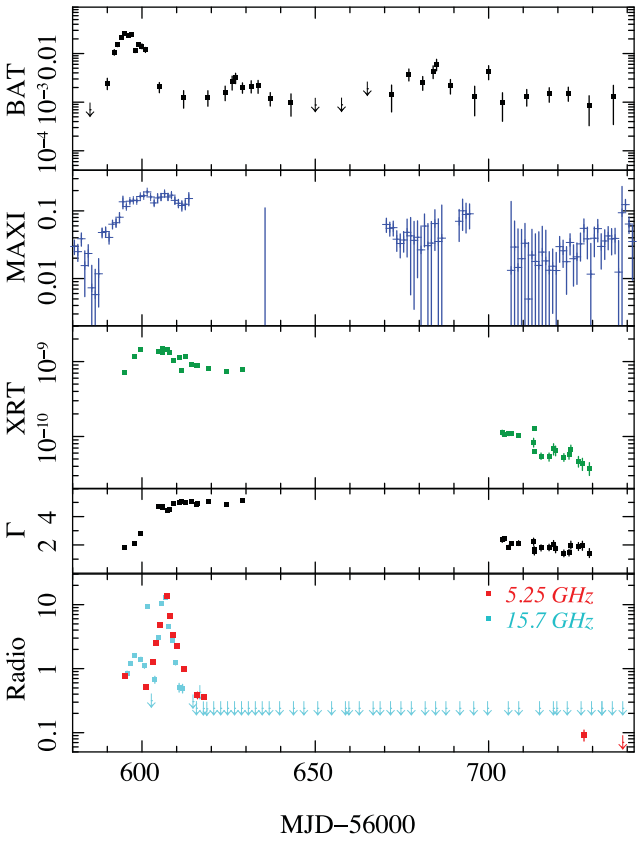

Figure 1. Hard (*Swift*/BAT 15–50 keV, counts/s) and soft (MAXI 2–20 keV, counts/s[6]; *Swift*/XRT 3–9 keV, erg cm^{-2} s^{-1}) X-ray light curves, X-ray photon index (Γ) and radio (5.25 and 15.7 GHz, mJy) light curves. Due to the source's proximity to the bright, persistent source GRS 1915+105, MAXI count rates may suffer from contamination, especially at low luminosities.

2.4 Polarization

We derived the polarization parameters at 5.25 and 7.45 GHz from the measured flux densities of the Stokes I, Q and U images (Table 1): linear polarization, LP $= \sqrt{Q^2+U^2}$; fractional polarization, FP $=$ 100LP/I; and polarization angle, PA $=$ 0.5 arctan(U/Q), which is degenerate such that derived angles may be offset by an integer multiple of $\pm 180^\circ$ from the true value. In the case of non-detections, the upper limit on polarimetry, P_{limit}, is calculated as three times the rms noise of the linear polarization over the field. The derived polarimetric parameters at 5.25 and 7.45 GHz are plotted in Fig. 2.

Faraday rotation in the local or interstellar medium causes a rotation of the polarization vectors at wavelength, λ, such that the intrinsic electric vector position angle (EVPA) of the source is related to the observed polarization angle, PA, by EVPA $=$ PA $-$ RMλ^2, where RM is the rotation measure (e.g. Saikia & Salter 1988). Given observed polarization angles, the RMs and EVPAs (plotted in Fig. 2) are derived from a linear fit of PA versus λ^2 for epochs where we were able to derive polarization angles at multiple wavelengths. Independent fitting of each epoch returned consistent RMs, with a weighted average of ≈775 rad m^{-2}. Applying a modified version of the simultaneous fit described by Curran et al. (2007), we find a common RM of 757 ± 16 rad m^{-2} and EVPAs that agree with those of the independent fits ($\chi^2_\nu = 1.2$; Fig. 3).

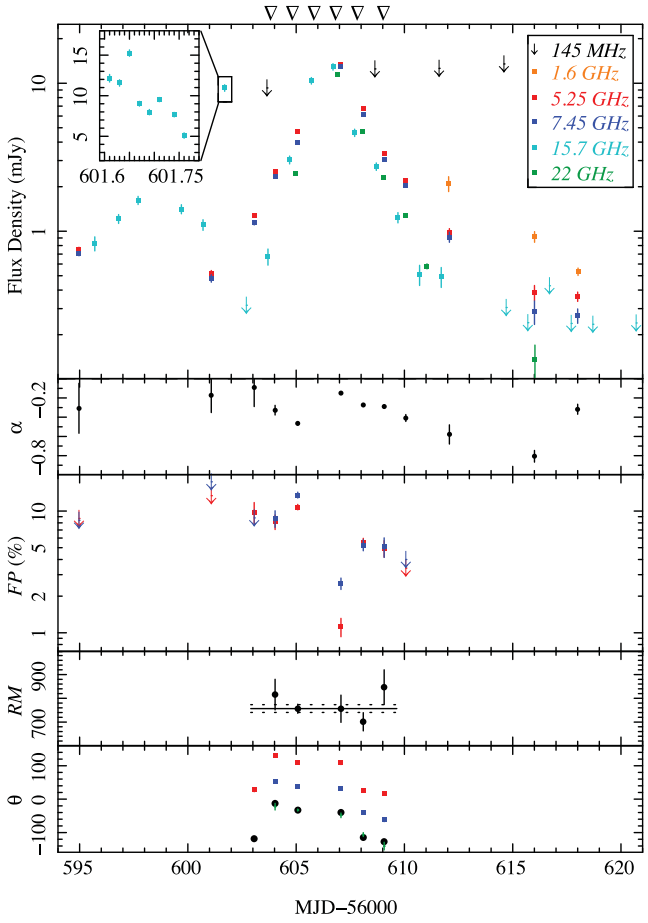

Figure 2. Radio light curves, spectral and polarization parameters of the source during the outburst. The upper panel shows the flux densities at each of the six radio frequencies observed (legend is common to all panels), while the inlay shows the time-resolved 15.7 GHz data from MJD 56601.7. The second panel shows the radio spectral index, α (where $F_\nu \propto \nu^\alpha$), while the third panel shows the fractional polarizations or limits, FP, at two frequencies (5.25 and 7.45 GHz; note that for clarity we only plot constraining limits, i.e. $\leq$20 per cent.). The fourth panel shows the rotation measure, RM, from independent (data points) and simultaneous (solid line with 1σ errors as dashed lines) fitting of the epochs. The fifth panel shows the observed polarization angles (blue and red) and the intrinsic electric vector position angle (EVPA), θ, derived from the independent (green) and simultaneous (black) fits of those PAs. The inverted triangles along the top axis represent the epochs of the VLBA observations reported in Rushton et al. (in preparation).

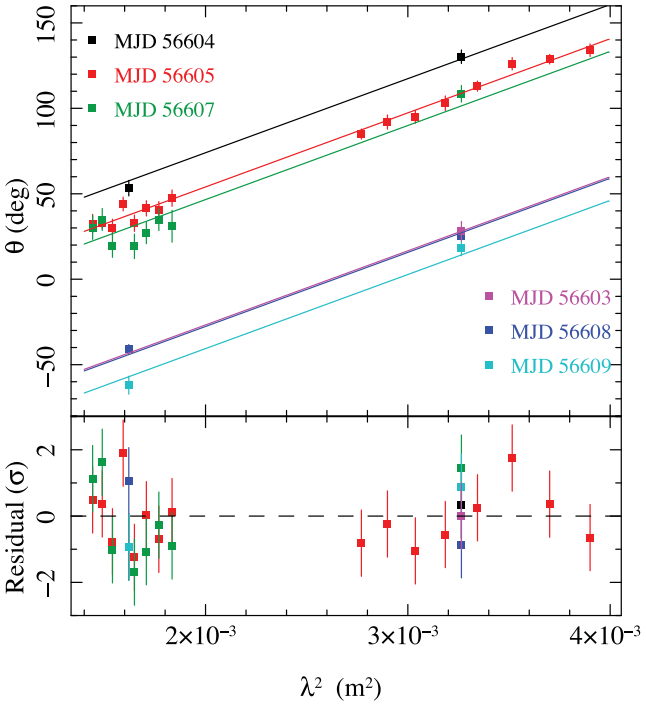

Figure 3. Plot of observed polarization angle versus wavelength, and simultaneous fit for the RM, for the six epochs with observed polarizations. The lower panel shows the residuals (in units of σ) from the simultaneous fit.

3 RESULTS AND DISCUSSION

3.1 Light curves and spectral indices

The broad-band light curves (Fig. 1) of the monitoring observations start to rise at MJD $\sim$ 56588–56590. Initially, these peak in the hard X-rays (15–50 keV), at MJD $\sim$ 56595, before fading by MJD 56610. The softer X-rays (2–20 keV) have a more gradual rise and decline, peaking at MJD $\sim$ 56601. By MJD $\sim$ 56675, after a period of the source being Sun-constrained, they had returned to the rms noise level of 0.0021 photons cm^{-2} s^{-1} (excluding outburst), though there may be hints of activity at later times. The 3–9 keV X-rays peak at MJD $\sim$ 56606 and decay to quiescence at MJD $>$ 56729, though there is a wide range of MJDs that are not sampled when the source was unobservable due to the position of the Sun.

The 5.25 and 7.45 GHz radio light curves (see also Fig. 2) peak at a similar time to the 3–9 keV X-rays, at MJD 56607, but have shorter rise and decay times of only $\sim$5 d. The higher cadence 15.7 GHz observations reveal a sharp flare, peaking at MJD $\sim$ 56601.7, at the same time as the peak in the 2–20 keV X-rays. This flare rises by almost an order of magnitude in a day and falls by a factor of at least 26 on the same time-scale. A time-resolved analysis of this data point (see inlay of Fig. 2) reveals significant variability over the 4 h observation, with an approximate decay consistent with the non-detection a day later.

During the X-ray flux rise the observed photon index increased from $\Gamma \sim 2$ to $\sim$5, where it remained until the Sun-constrained period. Noting that we were unable to fit a physically motivated model to the *Swift* spectra (Section 2.2), we define the soft state as the period when the photon index was $\sim$5; this definition is consistent both with the reported transition to a soft state at MJD $\sim$ 56598 (Negoro et al. 2013) and with the significant drop of hard (15–50 keV) X-ray photons at that time. When X-ray observations restarted, on MJD 56703, the photon index of our phenomenological fit was at a much lower value ($\Gamma < 2.5$), suggesting that the source had returned to a hard state, though the still-decreasing photon index indicates that the source was still hardening through to MJD 56730.

The observed radio spectra have indices, α, ranging from -0.1 to -0.8 (Fig. 2). Initially consistent with being optically thick ($\alpha \approx 0$), the indices steepen during the rise to maximum, at which point they flatten before again steepening with decreasing flux. The three initial spectral indices are ambiguous but the non-zero values could be consistent with the X-ray source transitioning to a soft state at MJD $\sim$ 56598 (Negoro et al. 2013). On seven epochs, we have low-frequency (145 MHz or 1.6 GHz) flux limits or detections. On the three epochs where we have 1.6 GHz fluxes, the spectra are consistent with a single (optically thin) spectral index at each epoch,

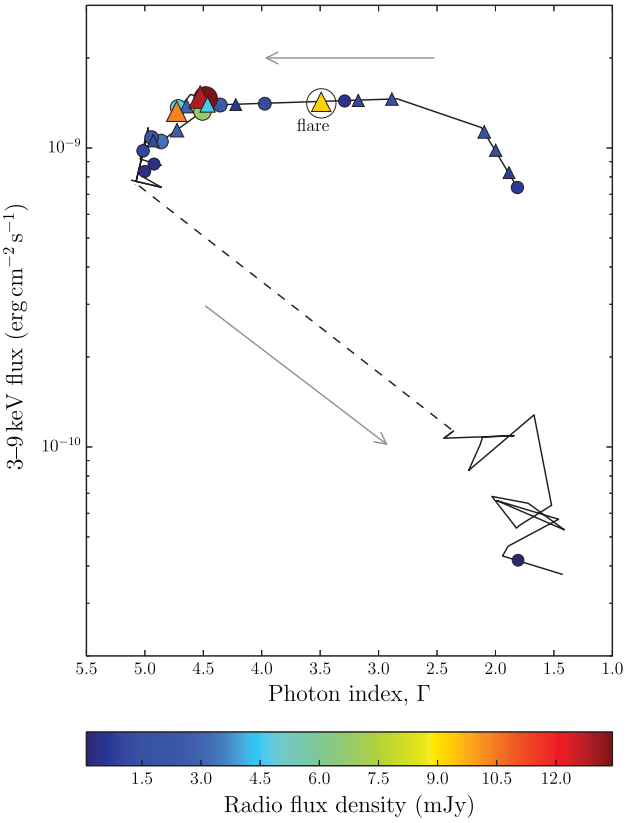

Figure 4. Proxy *Swift* HID (photon index versus flux) of the outburst, superimposed with 5.25 (circle) and 15.7 GHz (triangle) radio flux densities, with arrows representing temporal direction. The dashed line represents the period when X-ray observations were unavailable due to the source being Sun-constrained. The radio flux peaked in the soft (or possibly, late-intermediate) state while the sharp 15.7 GHz radio flare at MJD 56602 (circled) occurred during the intermediate state.

over the range of all observed frequencies (1.6–22 GHz). We have flux limits at 145 MHz on four epochs but only the 3σ limit on MJD $\sim$ 56609 is constraining, at a value of $\leq$12.5 mJy. Interpolating the 5.25, 7.45 and 22 GHz to the same epoch as our 145 MHz observations, and assuming a single power-law spectral index, indicates that XTE J1908+094 would have been detected at a level of $\approx 13 \pm 2$ mJy. While this is not inconsistent with the non-detection, closer inspection of the 145 MHz image reveals no candidate at a lower significance (formal value at position is -5 mJy), suggesting a possible break in the spectrum. The higher frequencies have a spectral index of $\alpha \approx -0.26 \pm 0.03$, consistent with optically thin emission from discrete ejecta, which suggests that the low-frequency emission at this time could be self-absorbed ($\alpha \approx +2.5$), as previously observed at $\sim$1 GHz for a discrete ejection of Cygnus X-3 (Miller-Jones et al. 2004). Future low-frequency observations from e.g. LOFAR or the Murchison Widefield Array will allow us to constrain the value and study the evolution of the spectral breaks over a wider range of frequencies than is currently possible and hence, in the case of compact jets, constrain the length of the jet.

3.1.1 Hardness–intensity

We plot the X-ray photon index versus the 3–9 keV flux as a proxy for the standard hardness–intensity diagram (HID in Fig. 4). This clearly shows that the source started in a hard state before quickly softening at constant flux before dimming at its softest. By the time the source emerged from being Sun-constrained (see Section 2.2), it had reverted to the hard state at a low luminosity. The source therefore followed the standard trajectory (e.g. Homan et al. 2001; Homan & Belloni 2005; Belloni 2010) through our proxy-HID.

Though the X-ray spectra do not allow us to unambiguously infer the states, the superimposed radio flux densities peak in either the late-intermediate or in the soft state, while the sharp radio flare, at MJD 56602, occurred during the intermediate state. Both of these radio flux maxima are consistent with the region associated with bright emission from a recent discrete ejection event (Fender 2006). The radio detection in the late, hard X-ray state indicates that the compact jet had been reestablished by MJD 56727, though due to limited VLA sampling and the AMI-LA flux limits it is unclear when it was reactivated. The 5.25–7.45 GHz spectral index at the time ($\alpha = 0.0 \pm 0.9$, Table 1) is unconstraining.

3.1.2 Comparison to 2002 outburst

The 2013 outburst of XTE J1908+094 lasted about 150 d (as observed by XRT), with a soft state of between 25 and 100 d. The total observed outburst is therefore significantly shorter than the 2002 (*RXTE*-observed) outburst (Göğüş et al. 2004), which lasted $\sim$400 d, staying active into 2003, though the duration of the soft state, lasting 60 d, could be comparable. Our rise time of $\sim$15–20 d is significantly quicker than the *RXTE*-observed rise times in 2002 of 50–80 d, though instrumental and energy-range differences will have a major effect. Overall however, the X-ray morphology displays no obvious differences. We observed a peak X-ray (3–9 keV) flux of $\approx 1.8 \times 10^{-9}$ erg cm^{-2} s^{-1} on MJD 56609. In 2002 the observed peak X-ray (2.5–25 keV) flux was 2.8×10^{-9} erg cm^{-2} s^{-1}, on MJD 52355 (Göğüş et al. 2004), which corresponds to $\approx 1.1 \times 10^{-9}$ erg cm^{-2} s^{-1} in the 3–9 keV range, assuming a power-law model.

It is difficult to directly compare the peak radio flux due to poor temporal sampling over the 2002 outburst. As our observations show (Fig. 2), without regular radio observations many radio flares may go undetected, i.e. the sharp radio flare at MJD 56602 was only detected in our 15.7 GHz observations and there was no evidence of it in our less frequent 5.25 GHz data. In 2002[2] the highest reported flux density was 1.8 mJy at 5.25 GHz, $\lesssim$10 times dimmer than our maximum flux density (13 mJy at 5.25 GHz) but consistent with most of our measurements, which are at the mJy level. Likewise, when we plot X-ray versus radio luminosity (Fig. 6; see Section 3.3), there is no difference between data from the two outbursts. We therefore find that there is no significant difference between either the X-ray or radio flux behaviour of the two outbursts, despite the fact that the resolved, discrete ejecta were observed $\sim$0.5 arcsec apart in 2002[2] and a factor of 10 less in 2013 (Rushton et al., in preparation).

3.2 Polarization

The radio emission at 5.25 and 7.45 GHz exhibits modest but variable levels of polarization of 1–14 per cent during the peak of the outburst (Fig. 2). At other epochs, we place upper limits on the fractional polarization but at MJDs $>$ 56611 these limits are over 20 per cent and are not constraining. The fractional polarization is at a minimum at the peak flux, on MJD 56607, though the absolute polarized flux density remains relatively constant throughout at 0.1–0.5 mJy so the minimum fractional polarization may be caused by the increase in total intensity. The derived RM of 757 ± 16 rad m^{-2}

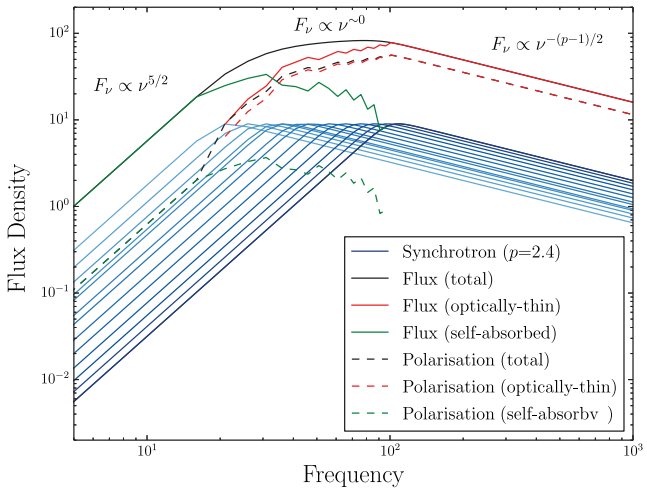

Figure 5. Schematic representation of the flux and polarization from a compact, partially self-absorbed jet demonstrating that the polarization of the flat spectrum is dominated by optically thin regions. The underlying distribution of the electron populations producing the individual synchrotron spectra is arbitrary, as are the flux and frequency units.

over all epochs is marginally higher than the RMs previously measured in this region, though those exhibit significant variation with $-600 \lesssim \mathrm{RM} \lesssim 600$ rad m^{-2} (Taylor, Stil & Sunstrum 2009; Kronberg & Newton-McGee 2011). The observed polarization angles and inferred EVPA exhibit a clear $\approx$90° rotation from $-120°$ on MJD 56603 to an average (though slightly decreasing) value of $-30°$ between MJDs 56604 and 56607; they are then observed to return to their original values on MJD 56608.

3.2.1 *EVPA and magnetic field*

Before we discuss XTE J1908+094, let us first consider the expected theoretical relationship between EVPA and magnetic field for both compact, partially self-absorbed, flat-spectrum jets and optically thin discrete ejecta. The radio emission originating from an optically thin discrete ejection is that of a single synchrotron spectrum while the emission from a compact, partially self-absorbed jet is a superposition of multiple synchrotron spectra (e.g. Blandford & Königl 1979; Hjellming & Johnston 1988), each with both optically thin and self-absorbed regions. Since $F_\nu \propto \nu^{+2.5}$ at self-absorbed frequencies and $F_\nu \propto \nu^{-(p-1)/2} \approx \nu^{-0.7}$ at optically thin frequencies (assuming a typical value of the electron energy distribution index, $p = 2.4$; e.g. Curran et al. 2010), the combined, flat spectrum (Fig. 5) will be dominated by emission from optically thin regions of the individual synchrotron spectra (e.g. Zdziarski et al. 2014). Assuming a uniform magnetic field, optically thin synchrotron emission is expected to have a maximum fractional polarization, $\mathrm{FP} \lesssim 100(p+1)/(p+7/3) \approx 72$ per cent while self-absorbed synchrotron emission, on the other hand, has $\mathrm{FP} \lesssim 300/(6p+13) \approx 11$ per cent (Longair 1994). The maximum fractional polarization is therefore expected to be $\mathrm{FP} \lesssim 72$ per cent for optically thin ejecta and a fraction of this, depending on the underlying electron populations, for compact, partially self-absorbed jets (Fig. 5). Likewise, while the EVPA of self-absorbed synchrotron emission is expected to be aligned parallel to the underlying magnetic field, the observed EVPA of a partially self-absorbed source will be dominated by optically thin emission, which is aligned perpendicular to the magnetic field (e.g. Ginzburg & Syrovatskii 1969; Longair 1994). Therefore, the EVPAs of both compact jets and discrete ejecta should be aligned perpendicularly to their magnetic fields.

Between MJDs 56604 and 5660, the observed EVPAs of XTE J1908+094 of $\approx -30°$ originate from a magnetic field perpendicular to the jet/ejection axis (north–north-west direction) observed in 2013 by both the VLBA and EVN, and, in 2002, by the VLA. These epochs coincide with the period when the VLBA clearly detected a dominant component moving to the south (Rushton et al., in preparation). In the simplest geometry of discrete ejecta, the dominant magnetic field is caused by shock compression (Laing 1980) and is parallel to the shock front (i.e. perpendicular to the jet axis). Our observations are hence consistent with such a strong forward shock in the southern component. It is also interesting to note that the EVPA decreases and deviates from the jet/ejection axis as the VLBA-observed southern component becomes spatially larger. This may indicate that magnetic field compression due to a forward shock becomes weaker as the ejection expands, allowing a differently orientated magnetic field to dominate the polarized emission.

The clear $\sim$90° rotation of the EVPA between MJDs 56607 and 56608, just after the peak of the flux, coincides with the fading of the southern component and the dominance of a new component moving to the north (Rushton et al., in preparation). Clearly, this discrete ejection does not follow the simple geometry described above but a more complex geometry due to, e.g., a complex magnetic field, lateral expansion, velocity shear, etc. (see Curran et al. 2014 and references therein). Without spatially resolved polarimetry, as has been obtained for both LMXBs (e.g. Miller-Jones et al. 2008) and, more commonly, AGN (e.g. Lister & Homan 2005; Gómez et al. 2008; Homan et al. 2009), it is not possible to determine which of these, if any, explain the non-standard magnetic field geometry.

Our initial EVPA, on MJD 56603, of $\approx -120°$ originates from a magnetic field aligned in the north–north-west direction, along the jet/ejection axis. It is unclear which of the two components, if either, this originates from since there is no resolved imaging at this time but it is unlikely that we are observing the compact jet. The X-ray photon index suggests that the source is already in a soft state and, while the radio data at this epoch are consistent with either a flat or an optically thin spectrum, the sharp radio flare, observed at 15.7 GHz on MJD $\sim$ 56602, is indicative of a transition to the soft state (Fender 2006).

Variable EVPAs, or 'rotator events', similar to the $\sim$90° rotations observed here have previously been observed in the LMXBs GRO J1655−40 (Hannikainen et al. 2000) and GRS 1915+105 (Fender et al. 2002), and in a number of AGN (see Saikia & Salter 1988, and references therein). They are thought to be caused by changes in the magnetic field or shock conditions but, as we have demonstrated, may also be due to different, unresolved components dominating the emission at different times.

3.3 Source distance

The transition from soft to hard states at the end of X-ray binary outbursts is observed to cluster at approximately 2 per cent of the Eddington luminosity (Maccarone 2003; Kalemci et al. 2013). While Dunn et al. (2010) find a significant spread of values from 0.5 to 10 per cent, using sources with poorly constrained masses and distances, Kalemci et al. (2013) find a much narrower spread from 1 to 3 per cent. Our observations do not cover the state transition itself but from X-ray fluxes in the soft and hard states (on MJDs 56629 and 56703) this transition must have occurred at a

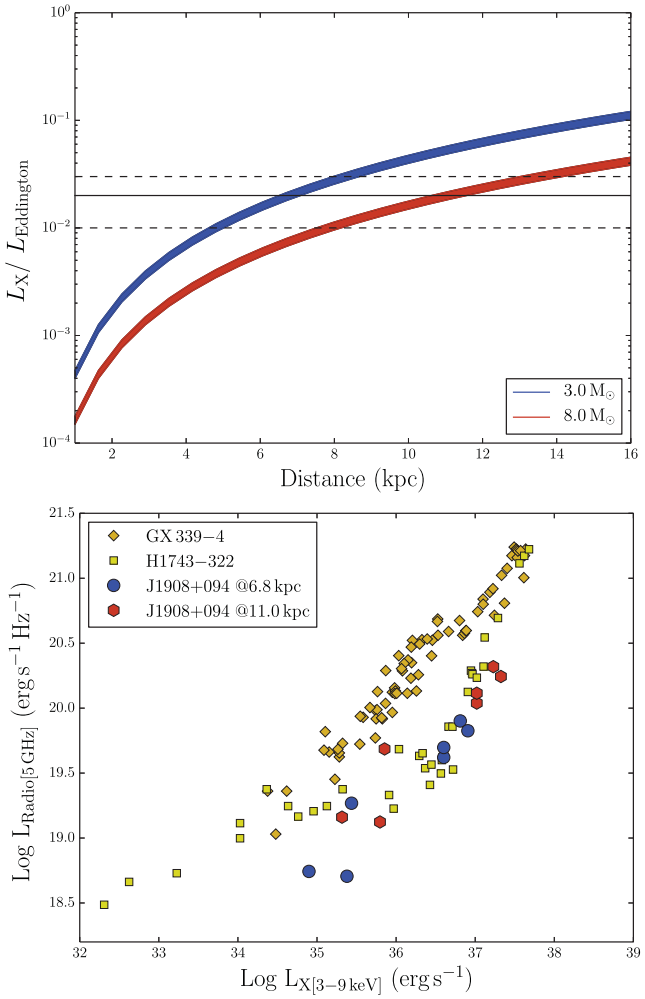

Figure 6. Upper panel: assuming that the source transitions from a soft to hard state at 2 per cent of the Eddington luminosity and a representative black hole mass of 8 $M_\odot$ (Kreidberg et al. 2012), the observed fluxes imply a source distance of 11 kpc (red), or, for a black hole mass of 3 $M_\odot$, 6.8 kpc (blue). Width of lines corresponds to uncertainty in observed flux at the state transition observed in 2002. Solid and dashed lines represent 2, 1 and 3 per cent of the Eddington luminosity. Lower panel: the hard state X-ray–radio luminosity correlation shows representative data from the upper (GX 339−4; Corbel et al. 2013) and lower (H1743−322; Coriat et al. 2011) branches, overlaid by our data for XTE J1908+094 at assumed distances of 6.8 and 11 kpc (the latter distance being more consistent with the representative data).

flux of within $\sim$1–8 $\times$ 10^{-10} erg cm^{-2} s^{-1} (3–9 keV). This is consistent with the transition flux of 4.2–5.0 $\times$ 10^{-10} erg cm^{-2} s^{-1} (2.5–25 keV) found by Göğüş et al. (2004) for the 2002 outburst of this source, at MJD 52425–52425. Converting the latter values to bolometric flux as in Maccarone (2003), i.e. assuming a spectrum of $dN/dE \propto E^{-1.8}\exp^{(-E/200\,keV)}$ integrated from 0.5 to 10^4 keV, we find that the transition occurs at $\approx$1.3 $\times$ 10^{-9} erg cm^{-2} s^{-1}. Assuming a representative black hole mass of 8 $M_\odot$ (Kreidberg et al. 2012), this implies that the distance to XTE J1908+094 is $\approx$11 kpc (7.8–13.6 kpc using the observed 1–3 per cent range of transition fluxes) or $\approx$6.8 kpc (4.8–8.3 kpc) for a black hole of 3 $M_\odot$ (Fig. 6).

While there is uncertainty (Gallo et al. 2014) as to whether the correlation between the X-ray and radio luminosities of LMXBs in the hard state (e.g. Hannikainen et al. 1998; Corbel et al. 2000, 2003, 2013; Gallo, Fender & Pooley 2003; Gallo, Miller & Fender 2012) is universal, it remains a useful diagnostic of source distance. In Fig. 6, we plot representative data from the upper (GX 339−4; Corbel et al. 2013, assuming, as they do, a distance of 8 kpc; Zdziarski et al. 2004) and lower (H1743−322; Coriat et al. 2011) branches. For comparison, we calculate the luminosities of XTE J1908+094 over/at the same energies as Corbel et al. and Coriat et al., at both 6.8 and 11 kpc (from above). Assuming a flat spectrum, we calculate the luminosity at 5 GHz from both our 5.25 and 15.7 GHz observations, for comparison with X-ray observations which occurred within 24 h. We also plot the 8.3 GHz radio flux on MJDs 52723.5 and 52741.5 (2003) from Jonker et al. (2004) and, using their spectral parameters, the interpolated 3–9 keV X-ray flux on 52722.0 and 52748.6. We did not extrapolate these data to a common epoch as any extrapolation will be insignificant within errors.

We find that the luminosities inferred assuming a source distance of 11 kpc are more consistent with the representative data of other black hole sources, though there is some scatter. Regardless of the source distance, XTE J1908+094 appears to fall on the lower, radio-quiet branch of the X-ray–radio flux relation (e.g. Coriat et al. 2011). The inconsistency of the 6.8 kpc data at low X-ray luminosities is caused by data from MJD 52741/8 (i.e. one of the 2003 points) and MJD 56727 (i.e. our late-time point); while the earlier point has a 7 d difference between observation epochs, the later point is based on data with only 11 h difference, during a period with little variability. 11 kpc is also consistent with the lower limit of $\gtrsim$6 kpc estimated from the peak bolometric flux in 2002 (in't Zand et al. 2002), as is 6.8 kpc. Though the optical extinction ($E(B-V) \approx 5.4$; Schlegel, Finkbeiner & Davis 1998) in that region (l, b = 43.°26, +0.°43) or derived, via Güver & Özel (2009), from our observed X-ray extinction ($2.2 \lesssim E(B-V) \lesssim 4.4$) is quite high, neither is inconsistent with the detection of a near-infrared counterpart at $\approx$11 kpc (Chaty et al. 2002, 2006).

4 CONCLUSIONS

We obtained multifrequency radio data of the LMXB and black hole candidate XTE J1908+094 from the VLA and AMI-LA arrays, spanning the entirety of its 2013 outburst. We also analysed the *Swift*/XRT X-ray data from this period and compared with the available MAXI and *Swift*/BAT X-ray light curves. We determine that the broad-band light curves, X-ray hardness–intensity and X-ray–radio flux relation are all consistent with XTE J1908+094 being a black hole LMXB. The source traced the standard hardness–intensity path, evolving from a hard state, through a soft state, before returning to a hard state. The radio behaviour is typical of a compact jet that becomes quenched and transitions to a discrete ejection at the late stages of X-ray softening (Fender 2006). We note that there is significant radio variability on time-scales of both hours and days and that this variability can only be observed with daily monitoring observations – without which many radio flares may go undetected. Neither the X-ray nor radio flux or light-curve morphology displayed any significant differences from the 2002 outburst of this source, despite the obvious difference in separation of the resolved, discrete ejecta between the two outbursts.

Radio polarization measurements allowed us to infer the jet orientation as being approximately in the north–north-west direction, in agreement with the resolved observations. We also observe a sharp 90° rotation of EVPA associated with a change of dominant component in resolved observations, as well as a lower level EVPA drift associated with the expansion of the ejecta reported elsewhere (Rushton et al., in preparation). Assuming that XTE J1908+094 is an 8 $M_\odot$ black hole, we estimate a distance of $\approx$11 kpc

(7.8–13.6 kpc) to the source, based both on the bolometric X-ray flux at the soft-to-hard transition and on the X-ray–radio flux relation. Regardless of the source distance, XTE J1908+094 is the newest addition to the lower, radio-quiet branch of the X-ray–radio flux relation (e.g. Coriat et al. 2011).

ACKNOWLEDGEMENTS

We thank the anonymous referee for constructive comments. We also thank T. J. Maccarone for useful discussions and A. M. M. Scaife for valuable input on the AMI-LA data. This work was supported by Australian Research Council grant DP120102393. DA acknowledges support from the Royal Society. GRS is supported in part by an NSERC Discovery Grant. SM is supported by the Spanish Ministerio de Ciencia e Innovación (grant AYA2013-47447-C03-1-P). This work was also supported in part by European Research Council Advanced Grant 267697 '4 Pi Sky: Extreme Astrophysics with Revolutionary Radio Telescopes'. The National Radio Astronomy Observatory is a facility of the National Science Foundation operated under cooperative agreement by Associated Universities, Inc. We thank the staff of the Mullard Radio Astronomy Observatory for their invaluable assistance in the operation of AMI-LA. LOFAR, the Low-Frequency Array designed and constructed by ASTRON, has facilities in several countries, that are owned by various parties (each with their own funding sources), and that are collectively operated by the International LOFAR Telescope (ILT) foundation under a joint scientific policy. This research has made use of NASA's Astrophysics Data System. *Swift*/XRT data were supplied by the UK Swift Science Data Centre at the University of Leicester, and *Swift*/BAT transient monitor results were provided by the *Swift*/BAT team.

REFERENCES

Anderson G. E. et al., 2014, MNRAS, 440, 2059
Belloni T. ed., 2010, in Lecture Notes in Physics, Vol. 794, The Jet Paradigm: From Microquasars to Quasars. Springer-Verlag, Berlin, p. 53
Blandford R. D., Königl A., 1979, ApJ, 232, 34
Brocksopp C., Miller-Jones J. C. A., Fender R. P., Stappers B. W., 2007, MNRAS, 378, 1111
Brocksopp C., Corbel S., Tzioumis A., Broderick J. W., Rodriguez J., Yang J., Fender R. P., Paragi Z., 2013, MNRAS, 432, 931
Chaty S., Mignani R. P., Vanzi L., 2002, IAU Circ., 7897, 2
Chaty S., Mignani R. P., Israel G. L., 2006, MNRAS, 365, 1387
Cohen A. S., Lane W. M., Cotton W. D., Kassim N. E., Lazio T. J. W., Perley R. A., Condon J. J., Erickson W. C., 2007, AJ, 134, 1245
Condon J. J., Cotton W. D., Greisen E. W., Yin Q. F., Perley R. A., Taylor G. B., Broderick J. J., 1998, AJ, 115, 1693
Corbel S., Fender R. P., Tzioumis A. K., Nowak M., McIntyre V., Durouchoux P., Sood R., 2000, A&A, 359, 251
Corbel S., Nowak M. A., Fender R. P., Tzioumis A. K., Markoff S., 2003, A&A, 400, 1007
Corbel S., Coriat M., Brocksopp C., Tzioumis A. K., Fender R. P., Tomsick J. A., Buxton M. M., Bailyn C. D., 2013, MNRAS, 428, 2500
Coriat M. et al., 2011, MNRAS, 414, 677
Coriat M., Tzioumis T., Corbel S., Fender R., 2013, Astron. Telegram, 5575, 1
Curran P. A. et al., 2007, A&A, 467, 1049
Curran P. A., Evans P. A., de Pasquale M., Page M. J., van der Horst A. J., 2010, ApJ, 716, L135
Curran P. A. et al., 2014, MNRAS, 437, 3265
Dunn R. J. H., Fender R. P., Körding E. G., Belloni T., Cabanac C., 2010, MNRAS, 403, 61
Fender R., 2003, Ap&SS, 288, 79
Fender R., 2006, in Lewin W. H. G., van der Klis M., eds, Cambridge Astrophysics Series, No. 39, Compact Stellar X-ray Sources. Cambridge Univ. Press, Cambridge, p. 381
Fender R. P., Rayner D., McCormick D. G., Muxlow T. W. B., Pooley G. G., Sault R. J., Spencer R. E., 2002, MNRAS, 336, 39
Gallo E., Fender R. P., Pooley G. G., 2003, MNRAS, 344, 60
Gallo E., Fender R. P., Miller-Jones J. C. A., Merloni A., Jonker P. G., Heinz S., Maccarone T. J., van der Klis M., 2006, MNRAS, 370, 1351
Gallo E., Miller B. P., Fender R., 2012, MNRAS, 423, 590
Gallo E. et al., 2014, MNRAS, 445, 290
Ginzburg V. L., Syrovatskii S. I., 1969, ARA&A, 7, 375
Göğüş E. et al., 2004, ApJ, 609, 977
Gómez J. L., Marscher A. P., Jorstad S. G., Agudo I., Roca-Sogorb M., 2008, ApJ, 681, L69
Güver T., Özel F., 2009, MNRAS, 400, 2050
Hannikainen D. C., Hunstead R. W., Campbell-Wilson D., Sood R. K., 1998, A&A, 337, 460
Hannikainen D. C., Hunstead R. W., Campbell-Wilson D., Wu K., McKay D. J., Smits D. P., Sault R. J., 2000, ApJ, 540, 521
Heald G. et al., 2011, J. Astrophys. Astron., 32, 589
Hjellming R. M., Johnston K. J., 1988, ApJ, 328, 600
Homan J., Belloni T., 2005, Ap&SS, 300, 107
Homan J., Wijnands R., van der Klis M., Belloni T., van Paradijs J., Klein-Wolt M., Fender R., Méndez M., 2001, ApJS, 132, 377
Homan D. C., Lister M. L., Aller H. D., Aller M. F., Wardle J. F. C., 2009, ApJ, 696, 328
in't Zand J. J. M., Miller J. M., Oosterbroek T., Parmar A. N., 2002, A&A, 394, 553
Jonker P. G., Gallo E., Dhawan V., Rupen M., Fender R. P., Dubus G., 2004, MNRAS, 351, 1359
Kalemci E., Dinçer T., Tomsick J. A., Buxton M. M., Bailyn C. D., Chun Y. Y., 2013, ApJ, 779, 95
Kreidberg L., Bailyn C. D., Farr W. M., Kalogera V., 2012, ApJ, 757, 36
Krimm H. A. et al., 2013a, ApJS, 209, 14
Krimm H. A. et al., 2013b, Astron. Telegram, 5523, 1
Krimm H. A., Kennea J. A., Holland S. T., 2013, Astron. Telegram, 5529, 1
Kronberg P. P., Newton-McGee K. J., 2011, PASA, 28, 171
Laing R. A., 1980, MNRAS, 193, 439
Lister M. L., Homan D. C., 2005, AJ, 130, 1389
Longair M. S., 1994, High Energy Astrophysics. Volume 2. Stars, the Galaxy and the Interstellar Medium. Cambridge Univ. Press, Cambridge
Maccarone T. J., 2003, A&A, 409, 697
McClintock J. E., Remillard R. A., 2006, in Lewin W. H. G., van der Klis M., eds, Cambridge Astrophysics Series, No. 39, Compact Stellar X-ray Sources. Cambridge Univ. Press, Cambridge, p. 157
McMullin J. P., Waters B., Schiebel D., Young W., Golap K., 2007, in Shaw R. A., Hill F., Bell D. J., eds, ASP Conf. Ser. Vol. 376, Astronomical Data Analysis Software and Systems XVI. Astron. Soc. Pac., San Francisco, p. 127
Matsuoka M. et al., 2009, PASJ, 61, 999
Miller-Jones J. C. A., Blundell K. M., Rupen M. P., Mioduszewski A. J., Duffy P., Beasley A. J., 2004, ApJ, 600, 368
Miller-Jones J. C. A., Migliari S., Fender R. P., Thompson T. W. J., van der Klis M., Méndez M., 2008, ApJ, 682, 1141
Miller-Jones J. C. A. et al., 2012, MNRAS, 421, 468
Miller-Jones J. C. A., Sivakoff G. R., Krimm H. A., 2013, Astron. Telegram, 5530, 1
Mirabel I. F., Rodríguez L. F., 1998, Nature, 392, 673
Negoro H. et al., 2013, Astron. Telegram, 5549, 1
Offringa A. R., van de Gronde J. J., Roerdink J. B. T. M., 2012, A&A, 539, A95
Paragi Z. et al., 2013, MNRAS, 432, 1319
Perrott Y. C. et al., 2013, MNRAS, 429, 3330
Rupen M. P., Mioduszewski A. J., Dhawan V., 2002, IAU Circ., 8029, 2
Rushton A. P., Fender R., Anderson G., Staley T., Rumsey C., Titterington D., 2013, Astron. Telegram, 5532, 1
Russell D. M., Shahbaz T., 2014, MNRAS, 438, 2083

Russell D. M., Miller-Jones J. C. A., Maccarone T. J., Yang Y. J., Fender R. P., Lewis F., 2011, ApJ, 739, L19
Russell T. D., Miller-Jones J. C. A., Curran P. A., Soria R., Russell D. M., Sivakoff G. R., 2015, MNRAS, 450, 1745
Saikia D. J., Salter C. J., 1988, ARA&A, 26, 93
Sault R. J., Teuben P. J., Wright M. C. H., 1995, in Shaw R. A., Payne H. E., Hayes J. J. E., eds, ASP Conf. Ser. Vol. 77, Astronomical Data Analysis Software and Systems IV. Astron. Soc. Pac., San Francisco, p. 433
Scaife A. M. M., Heald G. H., 2012, MNRAS, 423, L30
Schlegel D. J., Finkbeiner D. P., Davis M., 1998, ApJ, 500, 525
Staley T., Anderson G., 2015, Astrophysics Source Code Library, record ascl:1502.017
Staley T. D. et al., 2013, MNRAS, 428, 3114
Stirling A. M., Spencer R. E., Cawthorne T. V., Paragi Z., 2004, MNRAS, 354, 1239
Tasse C., van der Tol S., van Zwieten J., van Diepen G., Bhatnagar S., 2013, A&A, 553, A105
Taylor A. R., Stil J. M., Sunstrum C., 2009, ApJ, 702, 1230
Tingay S. J. et al., 1995, Nature, 374, 141
van der Horst A. J. et al., 2013, MNRAS, 436, 2625
van Haarlem M. P. et al., 2013, A&A, 556, A2
Webster W. J., Jr, Altenhoff W. J., Wink J. E., 1971, AJ, 76, 677
Woods P. M., Kouveliotou C., Finger M. H., Gogus E., Swank J., Markwardt C., Strohmayer T., 2002, IAU Circ., 7856, 1
Zdziarski A. A., Gierliński M., Mikołajewska J., Wardziński G., Smith D. M., Harmon B. A., Kitamoto S., 2004, MNRAS, 351, 791
Zdziarski A. A., Pjanka P., Sikora M., Stawarz Ł., 2014, MNRAS, 442, 3243
Zwart J. T. L. et al., 2008, MNRAS, 391, 1545

This paper has been typeset from a TEX/LATEX file prepared by the author.